



Experimental and Kinetic modeling of In-situ Catalytic (Fe/Cu) Pyrolytic Degradation of Water Hyacinth

Priyanka Yadav¹ · Sivamohan N. Reddy¹

Received: 6 December 2022 / Accepted: 18 September 2023 / Published online: 19 October 2023
© Akadémiai Kiadó, Budapest, Hungary 2023

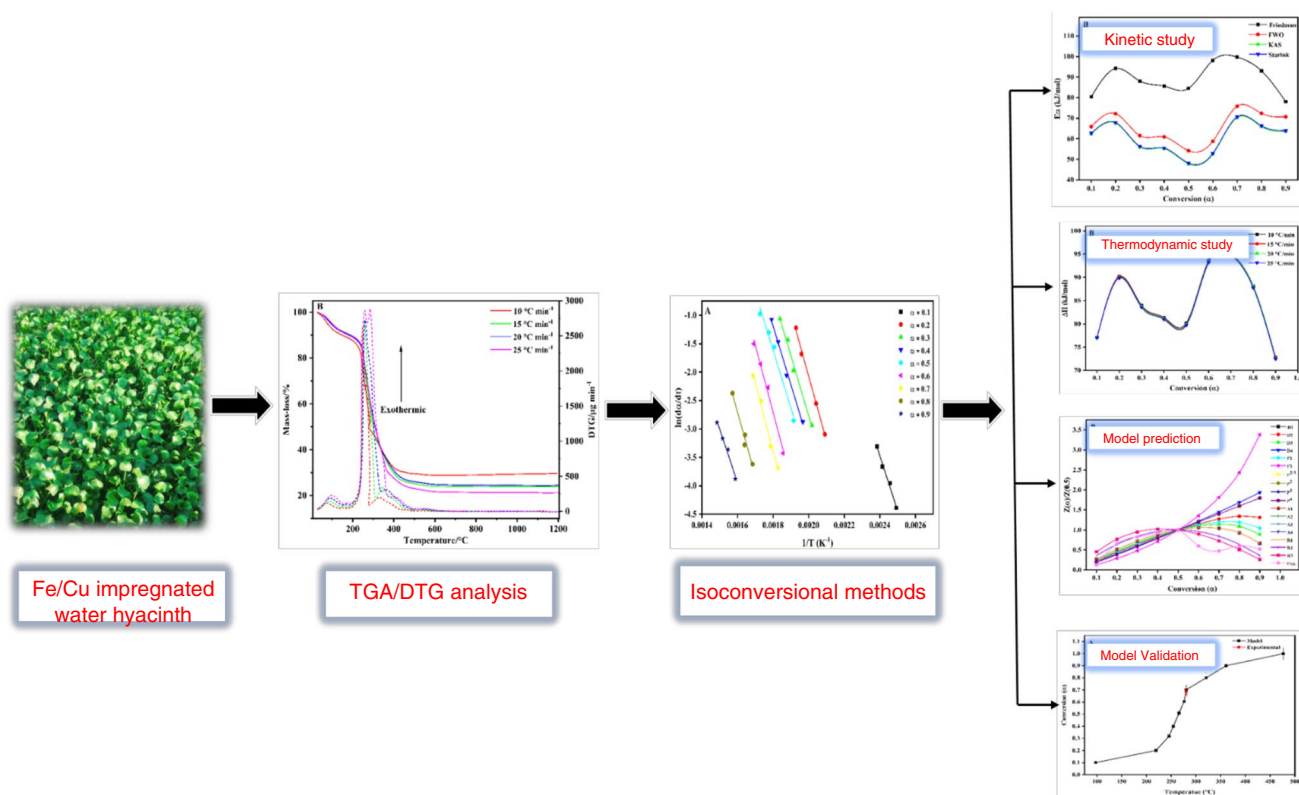
Abstract

Water hyacinth is recognized as a harmful plant, it extracts heavy metals from water bodies, and its disposal is quite challenging. The metal-impregnated samples can be effectively utilized to generate bio-oil and carbon hybrids by pyrolysis along with metal recovery in char. XRD, FESEM, and TEM analyzed the Fe/Cu-impregnated samples with an average particle size of 15.3 and 116 nm for Fe and Cu. Pyrolysis experiments were conducted at the optimum conditions to attain a maximum conversion of 68 and 48% for Fe and Cu-impregnated biomass and validated by kinetic modeling. The kinetic study of raw and metal-loaded samples was performed by modeling with Friedman, FWO, KAS, Kissinger, and Starink isoconversional processes at distinct heating rates of 10 to 25 °C min⁻¹ to estimate optimum conditions for pyrolytic conversion. The average activation energy for raw, Fe, and Cu-impregnated samples was maximum with the Friedman method 173.9, 89.1, and 97.4 kJ mol⁻¹, respectively. The metal-impregnated water hyacinth resulted in lower activation energy for reaction in comparison with the raw water hyacinth. The ΔH_{α} (168.9 kJ mol⁻¹) and ΔG_{α} (164.9 kJ mol⁻¹) are maximum for the raw water hyacinth in comparison with metal-impregnated samples, signifying the higher energy requirement for breaking reactant bonds. Model prediction was done by the Z-Master plot, which concluded that as the conversion (α) \leq 0.5, the thermal degradation follows the second- and third-order reaction mechanism, and a further increase in conversion (α) $>$ 0.5 follows the first-order reaction mechanism.

✉ Sivamohan N. Reddy
n.reddy@ch.iitr.ac.in

¹ Department of Chemical Engineering, Indian Institute of Technology Roorkee, Roorkee 247 667, Uttarakhand, India

Graphical abstract



Keywords Water hyacinth · Thermogravimetric analysis · Isoconversional models · Kinetic analysis

Abbreviations

WH	Water hyacinth
Cu-WH	Cu-impregnated water hyacinth
Fe-WH	Fe-impregnated water hyacinth
TGA	Thermogravimetric analysis
DTG	Derivative thermogravimetric
KAS	Kissinger–Akahira–Sunose
FWO	Flynn–Wall–Ozawa
DAEM	Simplified distributed activation energy method
E_a	Activation energy (kJ mol ⁻¹)
A	Frequency factor (s ⁻¹)
α	Degree of conversion
i	Temperature program (°C)
β	Heating rate (°C min ⁻¹)
ΔH_α	Change in enthalpy (kJ mol ⁻¹)
ΔG_α	Gibbs free energy (kJ mol ⁻¹)
ΔS_α	Change in entropy (kJ mol ⁻¹)

Introduction

The increase in the contribution of renewables to the energy mix has become mandatory to mitigate global warming. Today, bio-energy shares a major contribution to renewable energy in the world energy demand, and sustainable bio-energy requires biomass that is easily accessible and cheap. Lignocellulosic biomass is a renewable source comprising fragments namely cellulose, hemicellulose, and lignin to generate fuel. Cellulose (35–55%) is a linear polymer of repeating glucose units that are highly crystalline fibers that provide strength to the biomass [1–3]. Hemicellulose (20–35%) is a branched component of biomass which is a mixture of pentose and hexose sugars [4, 5]. Lignin (10–35%) is a cross-linked branched resin having an inexact molecular configuration [6]. It acts as a restrainer for the accumulation of cellulose units and protects against microbial and fungal attacks. Biofuels have some unsuitable properties such as thermal instability and lower heating value along with higher acidity, viscosity, gen, and nitrogen content which have limited the applicability of biofuels directly as a transportation fuel [7]. To improve their properties and

increase their usability commercially, biofuels are upgraded by various physio-chemical treatment methods such as esterification, catalytic cracking, hydro-treatment, emulsification, solvent addition, zeolite cracking, supercritical fluids, and steam reforming [8–11].

Water hyacinth (*Eichhornia crassipes*) is an aquatic plant and is considered a harmful weed as it grows faster and affects flora and fauna by depleting the oxygen and other nutrients from water bodies. Nowadays, research has focused on utilizing water hyacinth for the application of sustainable renewable energy and environment as it is inexpensive, easily available, and no competition with food crops for the production of biofuel, chemicals, bio-manure, bio-composites, effluent treatment, mushroom cultivation, and supercapacitors electrode development [12, 13] by combining assessment of various technologies namely, auto-control, machine-learning, process-modeling, and risk assessment in improvising the energy efficiency, phytoremediation wastewater reimplementation [14]. It has been reported that different heterogeneous catalysts have selectively promoted the yield of bio-oil. Various studies, namely, hydrothermal treatment of sugarcane bagasse with Cu/ γ -Al₂O₃-MgO [15], untreated and treated wood with copper, chromium, and boron (CCB) [16], hydrothermal liquefaction of Cu-impregnated fir sawdust with 91% of Cu recovery in the solid residue [17], hydrothermal liquefaction of water hyacinth in the presence of homogeneous catalysts [18], rice-straw [19] and sewage [20], were performed. Hydrothermal liquefaction experiments on coconut shells were conducted to study the effect of transition metals (CuCl₂, NiCl₂, and ZnCl₂) on bio-oil yields [21], and in another study [22], they performed the experiments with empty fruit bunches. In both studies, higher gaseous and lower bio-oil yields were reported. Research has also been done on the removal of metals namely, Cadmium, Copper, Nickel, and Zinc by investigating the absorption capacity of water hyacinth [23]. Water hyacinth roots were utilized for Cd and Zn removal [12] with a metal removal efficiency of 82–92 and 87–95%, respectively. Catalytic pyrolysis of sawdust reported the maximum H₂ yield of 172 mL g⁻¹ of biomass and syngas yield of 63% at 800 °C in the presence of calcined Fe/CaO catalyst due to additional secondary cracking and reforming reactions [24].

The recovery of metals from metal-loaded waste biomass and final disposal is quite challenging. Thermochemical conversion methods are widely adopted for the conversion of biomass into biofuel. The detailed knowledge of kinetic investigation with thermodynamic variables is a prerequisite in designing any reactor for the conversion of this metal-loaded biomass to fuels. Thermogravimetric analysis (TGA) is a thermal analytical approach to analyzing mass changes in the sample to time and temperature at a fixed heating rate in a controlled environment. It can be used as an effective

technique to study the decomposition kinetics for the prediction of the thermal degradation mechanism of metal-contaminated samples at different heating rates [25]. The performance of kinetic analysis was improved by employing the ETP method based on the kinetic compensation effect by using the Kissinger method [26]. The isoconversional model-free approach methods are more precise and accurate as compared to kinetic model fitting as the latter one resulted in more uncertainty in kinetic parameters estimation [27]. Isoconversional kinetic methods are divided into differential and integral models. The differential method has more accuracy and less intrinsic error as it is free from temperature integral but has a disadvantage in accurately calculating da/dt and da/dT terms. Friedman's isoconversional technique gained as the most popular differential model [28–30]. The integral method includes Flynn–Wall–Ozawa (FWO) linear isoconversional has an assumption of constant apparent activation energy during the reaction [31–34], Kissinger–Akahira–Sunose (KAS) linear isoconversional [35], and Kissinger isoconversional method [25, 36, 37]. The integral methods have the advantage of simplified calculation but have disadvantages of error due to approximations, Picard iteration requisite for temperature integral, and boundary conditions required for temperature integral are not accurately defined.

The kinetics of thermal degradation of metal-contaminated biomass and its impact on the degradation is specific for each metal. Moreover, different biomass has different kinetics because of the difference in their composition and compounds. As previously mentioned, water hyacinth has a good adsorption capacity for metals and these metals have the potential to act as a catalyst. Thus, the kinetics of thermal degradation are required to analyze the metal impregnation of biomass. The pyrolytic degradation of Fe/Cu-loaded water hyacinth was performed along with the characterization and quantification of the obtained products. The present paper conducted the thermogravimetric, kinetic, and thermodynamics parameters analysis of metal-loaded water hyacinth samples and compared them with raw water hyacinth. Pyrolysis experiments of Fe and Cu-impregnated water hyacinth were carried out at an optimum condition of 280 °C with 15 min residence time, and conversion results were compared with kinetic modeling. The investigation focused on TGA (Thermogravimetric Analysis) and DTG (Derivative Thermogravimetric) analysis. Kinetic study for non-isothermal analysis was done by various model-free approaches namely Friedman, Flynn–Wall–Ozawa (FWO), Kissinger–Akahira–Sunose (KAS), Kissinger, and Starink models for determining activation energy along with frequency factor. The differential method was chosen due to more accuracy, whereas integral methods were chosen due to the simplicity of calculations. A study of thermodynamic variables such as a change in enthalpy (ΔH), change in

entropy (ΔS), and Gibbs free energy (ΔG) was done by utilizing the Friedman kinetic isoconversional method. Friedman method was chosen for thermodynamic study as this method could be more accurate due to the temperature-free integral and minimal intrinsic error.

Materials and methods

Feedstock

Aquatic biomass water hyacinth was obtained through Sonali Puram canal (29°52'52"N 77°55'32"E) IIT Roorkee (Uttarakhand) to study thermogravimetric, kinetic, and thermodynamic parameters. Before the metal impregnation, water hyacinth was rinsed with tap water to discharge dirt particles and was chopped, ground in a mixer grinder then sieved by a 50 mesh screen sieve to obtain a particle size of less than 1 mm. Subsequently obtaining a uniform size of biomass, it was dried, followed by impregnation with cupric sulfate ($\text{CuSO}_4 \cdot 5\text{H}_2\text{O}$, 99.99% trace metal basis purity) and ferric chloride (FeCl_3 , 99.99% trace metal basis purity) to make the sample material for studies. Chemicals and other components required for experiments were ordered from Sigma-Aldrich, India.

Metal impregnation and experimental procedure

Metal salt solution of 0.1 M of $\text{CuSO}_4/\text{FeCl}_3$ was prepared for impregnation on water hyacinth separately. Impregnation was carried out with a 1:20 ratio of water hyacinth to metal salt solution kept on continuous stirring of 350 rpm for 24 h with pH adjustment after every 12 h to maintain the stable conditions. The metal-impregnated water hyacinth was filtered by Whatman filter paper and rinsed gently twice with 250 mL of Millipore water followed by drying the sample in an oven at 100 ± 5 °C to release the moisture. Further details about the feed preparation can be found in detail in our previous works. The amount of Fe/Cu loading onto the impregnated water hyacinth was determined by Microwave Plasma Atomic Emission Spectrometer (MPAES).

Pyrolysis of Fe & Cu-impregnated water hyacinth was executed at a temperature of 280 °C with high pressure (10 MPa) in a 300 mL Parr reactor having Model No. PARR 4843. In each experimental run, 4 g of impregnated sample was added to the reactor and purged with N_2 gas to maintain an inert atmosphere. The reactor was programmed for heating to the desired operating temperature and retained at that temperature for the specific reaction time. After the reaction, the products were collected and extracted with diethyl ether and evaporated to obtain light oil. Acetone was used to extract the heavy-oil components from the solid phase fraction that remained on filter paper and evaporated to quantify the heavy

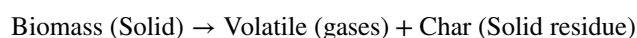
oil. The solid fraction that was leftover was designated as Fe/Cu carbon–metal hybrid. Each experimental run was performed thrice to compare the average yield conversion with the repeated kinetic simulation error bars.

Characterization and thermogravimetry

The Proximate analysis of raw and metal-impregnated water hyacinth (dry and ash-free basis) was carried out as per ASTM standards mentioned in our previous study. Elemental analysis of samples was performed using a VarioMICRO Cube CHNS analyzer. Quantitative metal (Fe/Cu) loading onto water hyacinth was estimated by Microwave Plasma Atomic Emission Spectroscopy Agilent, Model-4210. Surface morphology followed by the elemental configuration of samples was examined by the FESEM-EDX (Carl Zeiss Ultra Plus). Particle size dispersal in metal-loaded samples was investigated by Transmission electron microscopy (Model: S-TWIN FEI Tecnai G2 20). The crystallinity of metal-impregnated water hyacinth samples was examined by X-ray diffraction (Model: Bruker D8-Advance) with $\text{Cu-K}\alpha$ X-ray source anode having radiation at 0.154 nm of wavelength, and compounds in the XRD spectra along with the particle size were analyzed by X'Pert High score software. Thermal degradation of samples was determined by TGA/DTG analyzer (Model: SII 6300 EXSTAR) to determine the mass loss in samples to temperature. Approximately 10 ± 0.5 mg of sample was kept in the alumina crucible and heated from 25 to 1200 °C at a non-isothermal state at four distinct heating rates: 10, 15, 20, and 25 °C min^{-1} . The inert environment was sustained by purging N_2 at a flow rate of 200 mL min^{-1} . TGA/DTG output obtained by distinct heating rates was employed in determining kinetic parameters.

Kinetic parameters

The devolatilization of lignocellulosic biomass results in a single-step reaction mentioned below,



The general equation for the thermal decomposition of solid biomass is expressed by

$$\frac{d\alpha}{dt} = k(T)f(\alpha) \quad (1)$$

where $\frac{d\alpha}{dt}$ refers to the rate of conversion of biomass, α refers to conversion varying from 0 to 1, and $f(\alpha)$ refers to the function of conversion depending upon the reaction mechanism during the biomass decomposition.

$$\alpha = \frac{x_{\text{initial}} - x_t}{x_{\text{initial}} - x_{\text{final}}} \quad (2)$$

Conversion α is evaluated based on the mass of samples thermally degraded about time/temperature, where x_{initial} is initial dry mass, x_{final} is final dry mass and x_t is the mass of the sample at any time t .

The reaction-rate constant term, $k(T)$, is evaluated by utilizing Arrhenius expression as;

$$k(T) = A \cdot \exp\left(\frac{-E_\alpha}{RT}\right) \tag{3}$$

where A represents the frequency factor, E_α refers to the activation energy, R is the universal gas constant and T is the reaction temperature (kelvin).

Now, substituting the expression of $k(T)$ from Eq. (2) to Eq. (1), the following expression will be obtained,

$$\frac{d\alpha}{dt} = A \cdot \exp\left(\frac{-E_\alpha}{RT}\right) f(\alpha) \tag{4}$$

The resulting expression is valid for both isothermal as well as non-isothermal temperature conditions. In case of non-isothermal conditions at a constant heating rate ($\beta(K\text{min}^{-1}) = dT/dt$), the reaction rate is expressed as,

$$\frac{d\alpha}{dT} = \frac{A}{\beta} \cdot \exp\left(\frac{-E_\alpha}{RT}\right) f(\alpha) \tag{5}$$

The integrated form of the reaction mechanism (expression (5)) is written as:

$$g(\alpha) = \int_0^\alpha \frac{d\alpha}{f(\alpha)} = \frac{A}{\beta} \int_{T_0}^T \exp\left(\frac{-E_\alpha}{RT}\right) dt = \frac{AE_\alpha}{\beta R} p(x) \tag{6}$$

Here, $p(x)$ corresponds integral of temperature and it does not have any precise analytical result. It can only be solved by numerous interpolation equations based on approximations. The integrated form of the conversion mechanism, $g(\alpha)$ depends upon the function $f(\alpha)$. Different kinetic models were studied based on the above equations.

Estimation of activation energy

The activation energy was determined by both differential (Friedman method) and integral isoconversional models, such as FWO, KAS, Starink, and Kissinger method.

Differential isoconversional model Friedman model: It is the first isoconversional model-free model where the differential form of the kinetic model is applicable. The expression introduced by Friedman is represented as

$$\ln\left(\frac{d\alpha}{dt}\right)_{\alpha,i} = \ln[f(\alpha)A_\alpha] - \frac{E_\alpha}{RT_{\alpha,i}} \tag{7}$$

The activation energy (E_α) can be determined by the slope of the plot of $\ln[(d\alpha/dT)_{\alpha,i}]_{\alpha,i}$ vs. $-1/T_{\alpha,i}$ using Eq. (7), at a constant conversion (α).

Integral isoconversional models In the case of isothermal conditions at a constant heating rate (β) the equation for the integral isoconversional method is expressed as

$$g(\alpha) = \frac{A}{\beta} \int_{T_0}^T \exp\left(\frac{-E_\alpha}{RT}\right) dt = \frac{AE_\alpha}{\beta R} p(x) \tag{8}$$

Term $p(x)$ is based on the mathematical assumption and does not have any analytical solution. FWO, KAS, Kissinger, and Starink methods are integral isoconversional models employed for determining activation energy along with frequency factors.

Flynn–Wall–Ozawa (FWO) FWO model applied Doyle’s approximation in determining the integral of temperature as

$$p(x) = \exp(-2.315 - 0.4567x), \text{ for } 20 \leq x \leq 60 \tag{9}$$

Incorporating Doyle approximation (Eq. (9)) in Eq. (8) results in the following expression as

$$\ln(\beta_i) = \ln\left(\frac{AE_\alpha}{Rg(\alpha)}\right) - 5.331 - 1.052 \frac{E_\alpha}{RT} \tag{10}$$

In Eq. (10), the term $\ln(AE_\alpha/Rg(\alpha))$ is constant; hence, expression can be simplified to

$$\ln(\beta_i) = \text{Const.} - 1.052 \frac{E_\alpha}{RT_{\alpha,i}} \tag{11}$$

E_α can be determined by the slope of $\ln(\beta_i)$ against $1/T_{\alpha,i}$ plot for each conversion (α) value. The subscripts α and i correspond to the conversion at a corresponding heating rate value, respectively.

Kissinger–Akahira–Sunose (KAS) Kissinger–Akahira–Sunose (KAS) model adopted Murray and White approximation and expressed it as

$$\log p(x) \cong \left(\frac{\exp^{-x}}{x^2}\right), \text{ for } 20 \leq x \leq 50 \tag{12}$$

After assuming the exponential term (Eq. (12)) and rearranging the term in Eq. (8) resulted in the following expression as

$$\ln\left(\frac{\beta_i}{T_{\alpha,i}^2}\right) = \ln\left(\frac{AR}{E_\alpha g(\alpha)}\right) - \frac{E_\alpha}{RT_{\alpha,i}} \tag{13}$$

At any α value, the E_α can be determined by the slope of $\ln(\beta_i/T_{\alpha,i}^2)$ against $1/T_{\alpha,i}$.

Starink method For estimating the activation energy more accurately, Starink proposed a method similar to the previously mentioned integral isoconversional methods. Starink method also depends on calculating the slope of the logarithmic function consisting of heating rate β_i versus $1/T_i$ at any α [25]. Starink's expression is expressed as:

$$\ln\left(\frac{\beta_i}{T_{\alpha,i}^{1.92}}\right) = \text{Const.} - 1.008\left(\frac{E_\alpha}{RT_{\alpha,i}}\right) \quad (14)$$

E_α can be examined by the slope of the plot of $\ln(\beta/T^{1.92})$ versus $1/T$.

Kissinger Kissinger introduced the first model in 1956, to evaluate E_α in non-isothermal systems. This model assumed that at a given conversion (α) value, the activation energy (E_α) is constant and is expressed as

$$\ln\left(\frac{\beta}{T_{\max}^2}\right) = \ln\left(\frac{AR}{E_\alpha}\right) - \frac{E_\alpha}{RT_{\max}} \quad (15)$$

E_α can be evaluated by the slope of the plot $\ln(\beta/T_{\max}^2)$ against $1/T_{\max}$, where, T_{\max} (DTG peak temperature).

Determination of frequency factor

Kissinger's model is inapplicable in determining the activation energy because of its limitation as it is assumed on various heating rates, although it gives the constant value of activation energy for the overall conversion procedure. Hence, activation energy (E_α), calculated at every conversion value by Friedman, FWO, KAS, and Starink models can be utilized in calculating frequency factor (A), according to Kissinger's method by the following expression as mentioned below

$$A = \frac{\beta E_\alpha \exp(E_\alpha/RT_{\max})}{RT_{\max}^2} \quad (16)$$

Thermodynamic variables

The feasibility of any system is defined by thermodynamic variables, namely, change in enthalpy, Gibbs-free energy change, and change in entropy were estimated utilizing expressions (17) to (19). The change in enthalpy (ΔH_α) is energy variation between reactant and activated intermediate. Change in entropy (ΔS_α), the degree of disorder or

arrangement of carbon atoms in the reaction system. The negative value indicates the formation of thermally stable products, whereas the positive value indicates the thermally unstable products. The Gibbs-free energy change (ΔG_α) is excess energy required by the system to form an activated complex.

$$\Delta H_\alpha = E_\alpha - RT_\alpha \quad (17)$$

$$\Delta G_\alpha = E_\alpha + RT_m \ln\left(\frac{k_B T_m}{h A_\alpha}\right) \quad (18)$$

$$\Delta S_\alpha = \frac{\Delta H_\alpha - \Delta G_\alpha}{T_m} \quad (19)$$

Here, k_B is Boltzmann constant ($1.38064852 \times 10^{-23} \text{ m}^2 \text{ kg s}^{-2} \text{ K}^{-1}$), h is planks constant ($6.62607004 \times 10^{-34} \text{ m}^2 \text{ kg s}^{-1}$), T_m is DTG peak temperature.

Z-Master-plot method

The Z-Master plots approach was implemented in predicting the reaction kinetic model, $f(\alpha)$ by correlating theoretical with experimental master plots at specified activation energy value, E_α . The experimental master plots can be determined by

$$Z(\alpha) = \frac{AE}{\beta R} P(u) \quad (20)$$

where $P(u)$ is expressed as:

$$P(u) = \int_{\infty}^{\alpha} -\left(\frac{e^{-u}}{u^2}\right) du \quad (21)$$

where $u = E/RT$.

Doyle's approximation is utilized to attain the expression for $P(u)$. By taking reference as $x=0.5$ in Eq. (20), we will get

$$Z(0.5) = \frac{AE}{\beta R} P(u_{0.5}) \quad (22)$$

Now, dividing equation by equation we get,

$$\frac{Z(\alpha)}{Z(0.5)} = \frac{P(u)}{P(u_{0.5})} \quad (23)$$

$$\frac{P(u)}{P(u_{0.5})} = \frac{T^2 \exp(-E/RT)}{T_{0.5}^2 \exp(-E/RT_{0.5})} \quad (24)$$

The expression (24) is utilized to plot experimental curves at the different heating rates and compared with

the curves obtained by Eq. (23) for each kinetic model to predict the mechanism involved in the thermal degradation process.

Results and discussion

Biomass characterization

Proximate and ultimate analysis

The proximate and ultimate study of raw and metal (Cu & Fe) loaded water hyacinth is shown in Table S2 (Supplementary File). Feedstock showed a high value of ash content (16.23%), which is attributed to the presence of silica in water hyacinth. A higher value of volatile matter (71.8%) was noted, the amount during the vaporization of condensable and non-condensable matter during thermal degradation [31]. The lower value of fixed carbon (12%) is the indication of lower lignin content in biomass. The ultimate analysis results revealed that the amount of hydrogen content was in the range of 3.8–4.3% which is on par with results available in the literature [12]. The amount of carbon and oxygen gets reduced in metal-impregnated biomass samples as compared to raw samples as the ion exchange of biomass elements with the metal salt (Cu, Fe) during impregnation resulted in the loss of organic extractives and the addition of metals onto the biomass.

MP-AES analysis

The pH drift method was employed in determining the pH value at a zero-point charge (pH_{ZPC}) for both metal-impregnated (Cu & Fe) water hyacinths. The quantitative loading of the metals along with other key elements by MP-AES analysis confirms the displacement of alkali (Na & K) and alkaline earth (Mg & Ca) metals with the Fe/Cu metal in the impregnated water hyacinth sample. In the Fe-impregnated sample, Fe metal loading increased to 92,730 from 580 (ppm), while the concentration of alkaline metals and alkaline earth metals, K & Na reduced to 10,923.8 and 4420.6 from 59,081.1 and 25,503.5 (ppm) concentration, respectively, and Mg and Ca to 2630.4 and 13,449.7 from 9259.5 and 21,032.9 (ppm) concentration, respectively. The Cu metal loading increases to 22.91 (ppm), whereas the concentration of univalent metals such as K and Na decreases from 16.36 to 0.27 and 1.91 to 0.42 ppm, respectively, along with the decrease in the concentration of di-cationic metals (Mg, Ca) from 1.13 to 0.19 and 9.15 to 3.15 (ppm). In the case of the Fe-impregnated biomass sample, the pH_{ZPC} was found to be

at pH 4.7 with the maximum metal loading of 1.66 mol of Fe kg of biomass⁻¹ [38], whereas in Cu-impregnated water hyacinth the pH_{ZPC} was at pH 5.2 with the maximum loading of 0.72 mol of Cu kg of biomass⁻¹.

FESEM and TEM analysis

FESEM-EDX (Field Emission Scanning Electron Microscopy) analysis was performed to analyze the surface structure and quantitative dispersion of metal particles on water hyacinth at 20 μm to 100 nm. FESEM images followed by EDX for metal dispersion of raw water hyacinth, Fe and Cu-impregnated water hyacinth are shown in Fig. 1. FESEM captured the images of raw-water hyacinth that is smooth and porous in structure whereas, after the metal impregnation, Fe-impregnated shows the rugged and uneven nature having white dots of metal particles distributed onto the water hyacinth. Similarly, the Cu-impregnated biomass shows a rugged structure along with white Cu nanoparticles onto the water hyacinth. The EDX of raw water hyacinth shows 52.8 atomic% and 45.7 mass% of carbon, 47.2 atomic% and 54.3 mass% of oxygen, whereas this carbon and oxygen mass percent declines in the Fe and Cu-impregnated water hyacinth to raw water hyacinth as result of metal loading. The quantification of metal absorption was estimated by using EDX which results in 3.48 atomic% and 12.45 mass% of Fe in Fe-impregnated biomass, whereas EDX of Cu-impregnated water hyacinth shows the 1.87 atomic% and 7.99 mass% Cu loading on water hyacinth.

TEM analysis was performed at a magnification of 500 nm for analyzing the shape and size of metal particles by ImageJ software. Figure 2 shows the TEM images of Fe and Cu-impregnated water hyacinth samples along with particle size distribution. TEM images of Fe (Fig. 2a) and Cu (Fig. 2d) loaded water hyacinth showed the black spherical dots representing the metal particles that were formed at the time of impregnation, respectively. The SAED (selected area electron diffraction pattern) examined the crystalline arrangement of metal-loaded water hyacinth samples and signified a continuous diffused ring with bright white spots confirming polycrystalline structure in metal-impregnated water hyacinth samples. Average metal particle size resulted in 15.3 and 116 nm in Fe-impregnated and Cu-impregnated water hyacinth samples, respectively, by the particle size distribution histogram as shown in Fig. 2c and f.

XRD analysis

The crystallinity in samples was examined by XRD analysis, and spectra were examined by employing X'Pert High Score software. XRD patterns of metal-impregnated water hyacinth samples obtained after the impregnation and carbon material after pyrolysis are shown in Fig. 3.

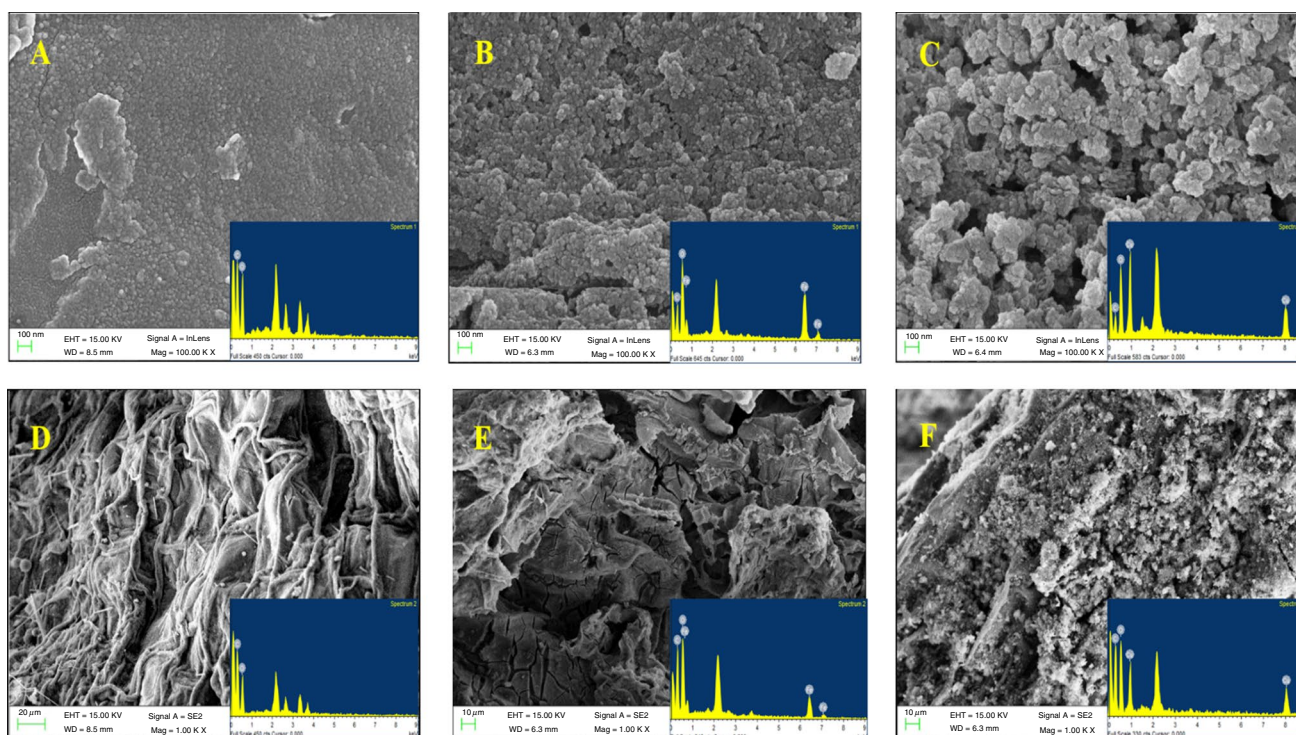


Fig. 1 FESEM images of **a** Raw water hyacinth, **b** Fe-impregnated water hyacinth, and **c** Cu-impregnated water hyacinth at 100 nm and 20 μm

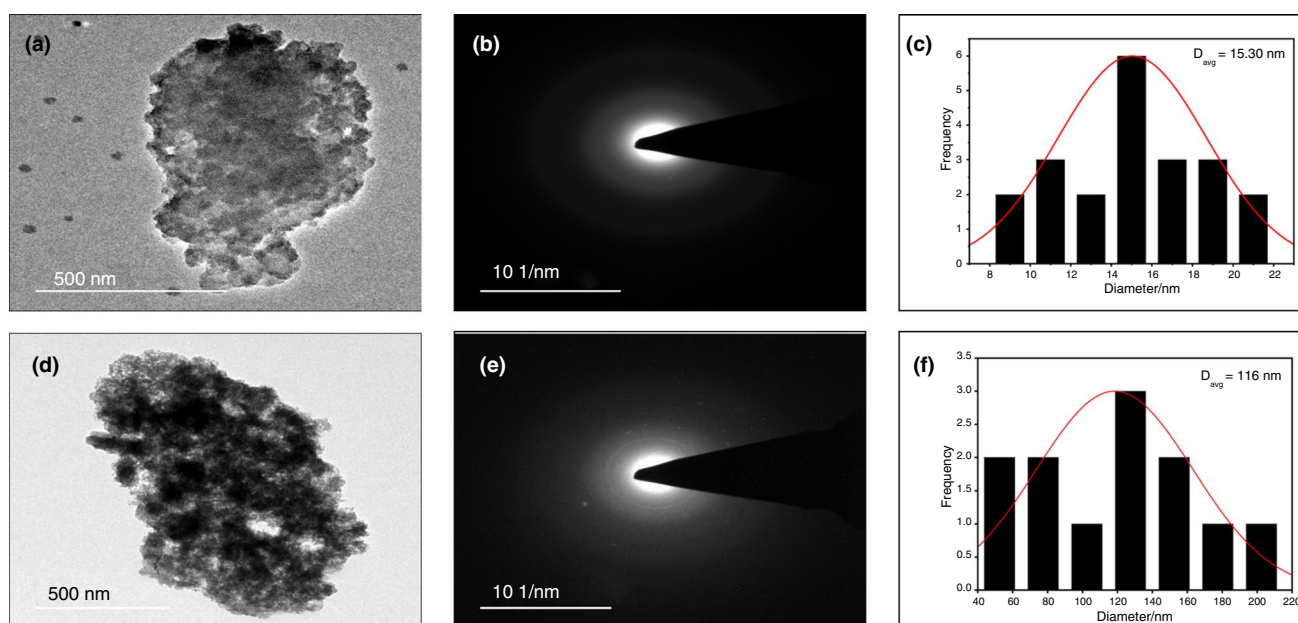


Fig. 2 TEM images of **a** Fe-impregnated water hyacinth, **b** SAED pattern, **c** particle size distribution, **d** Cu-impregnated water hyacinth, **e** SAED pattern, and **f** particle size distribution

Fe and Cu-impregnated water hyacinth samples in Fig. 3a initially show diffraction crystalline peak of cellulose in nature. The intensity between 8° and 17° of 2θ values was mainly the result of cellulose present in the biomass [39].

Fe-impregnated biomass then shows the crystalline peaks at 2θ values of $\sim 32.17^\circ$, 46.03° , 57.07° , 75.82° , and 84.79° for Fe_2O_3 (JCPDS-ICDD File No.-39-1346). For Fe_3O_4 (JCPDS-ICDD File No.-19-0629) diffraction peaks were

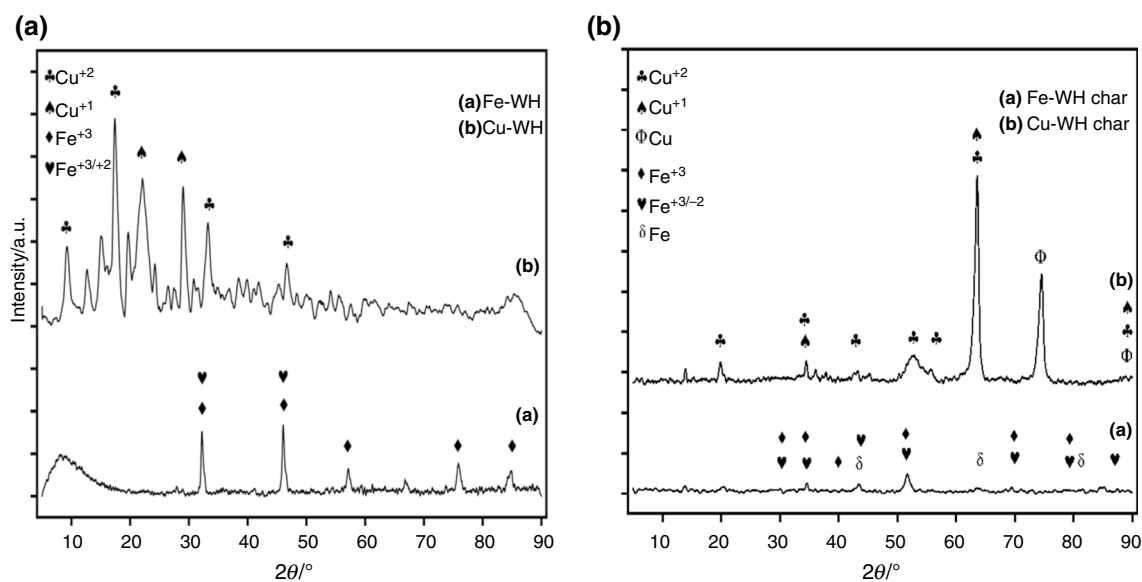


Fig. 3 XRD pattern of **a** Fe and Cu-impregnated water hyacinth and **b** Fe and Cu-carbon nanometals

mainly present at 2θ values of $\sim 32.17^\circ$, 46.03° , and 66.89° . The crystalline nature of cellulose present in the biomass is converted to amorphous nature due to the impregnation of maghemite on biomass [39]. In the case of the Fe-impregnated sample, XRD diffraction peaks were mainly present in Fe (+3) and Fe (+2) oxidation states in hydrated/oxide forms. Cu-impregnated biomass then shows the crystalline peaks at 2θ values of $\sim 17.27^\circ$, 33.29° , and 46.63° for CuO (Cu^{+2}) matching with the JCPDS-ICDD file no. 00-044-0706. For Cu_2O (Cu^{+1}) with the JCPDS-ICDD file no. 00-005-0667 single diffraction peak was present at a 2θ value of $\sim 28.90^\circ$. In the Cu-impregnated water hyacinth sample, diffraction peaks were mainly due to the existence of Cu^{+2} . The average particle size as calculated by the Debye Scherrer equation resulted in 16.2 nm and 110 nm for Fe and Cu-impregnated water hyacinth samples, respectively. These XRD results of impregnated samples are in good agreement with TEM results as discussed above.

Figure 3b shows the XRD spectra of Fe and Cu-carbon nanometals obtained by pyrolysis experiments. Nano-Fe-carbon material shows the crystalline peaks at 2θ values of $\sim 30.02^\circ$, 35.50° , 40.30° , 70.82° , and 79.53° for Fe_2O_3 , whereas, for Fe_3O_4 diffraction peaks were mainly present at 2θ value of $\sim 30.02^\circ$, 35.50° , 44.32° , 51.62° , 70.82° , and 87.50° . It also shows the peaks of nanometal Fe (Fe^0) at 2θ values of $\sim 44.74^\circ$, 65.10° , and 82.18° matching with the JCPDS-ICDD file no. 00-006-0696. Cu-nano-carbon material shows crystalline peaks at 2θ values of $\sim 19.71^\circ$, 34.54° , 43.16° , 53.39° , 56.64° , 63.48° and 89.75° for CuO (Cu^{+2}) and Cu_2O (Cu^{+1}) diffraction peak was present at 2θ value of $\sim 34.54^\circ$, 63.48° , and 89.75° . In Cu-impregnated water hyacinth diffraction, peaks were mainly due to the existence

of a Cu^{+2} . Cu shows the crystalline peaks at a 2θ value of $\sim 73.99^\circ$, and 89.75° for nanometal Cu^0 matching with the JCPDS-ICDD file no. 00-004-0836. The average particle size as calculated by the Debye Scherrer equation resulted in 36.7 and 57.1 nm for Fe and Cu carbon material, respectively. Due to the reactive nature of iron nanoparticles, they tend to oxidize and agglomerate easily which results in an increase in particle size in Fe–metal–carbon particles.

Thermal analysis

TGA analysis was conducted to examine the thermal degradation behavior of samples under a nitrogen atmosphere. Figure 4 shows the TGA curves of raw water hyacinth, Fe-impregnated, and Cu-impregnated water hyacinth samples each at distinct heating rates of $10\text{--}25^\circ\text{C min}^{-1}$. Thermal degradation of all samples started at around 50°C and maximum mass loss in the first dip was observed between 70 and 120°C , which is due to the rapid loss of moisture and light volatiles. The maximum mass loss was observed in the second dip between 200 and 300°C , as water hyacinth is hemicellulosic biomass and the devolatilization region corresponds to the disintegration of these biomass monomers by following cleavage, deamination, decarboxylation, and dehydration reactions to the bio-oil formation [40, 41]. The stagnant mass loss until 350°C is due to the recombination and re-polymerization of reactive fragments remaining resulting in the formation of carbon material [42]. The final residual masses of raw water hyacinth and metal-impregnated water hyacinth at 900°C were in the range of $18\text{--}22\%$ of the initial mass, with the metal-impregnated water hyacinth having a higher residual fraction as compared to raw water hyacinth.

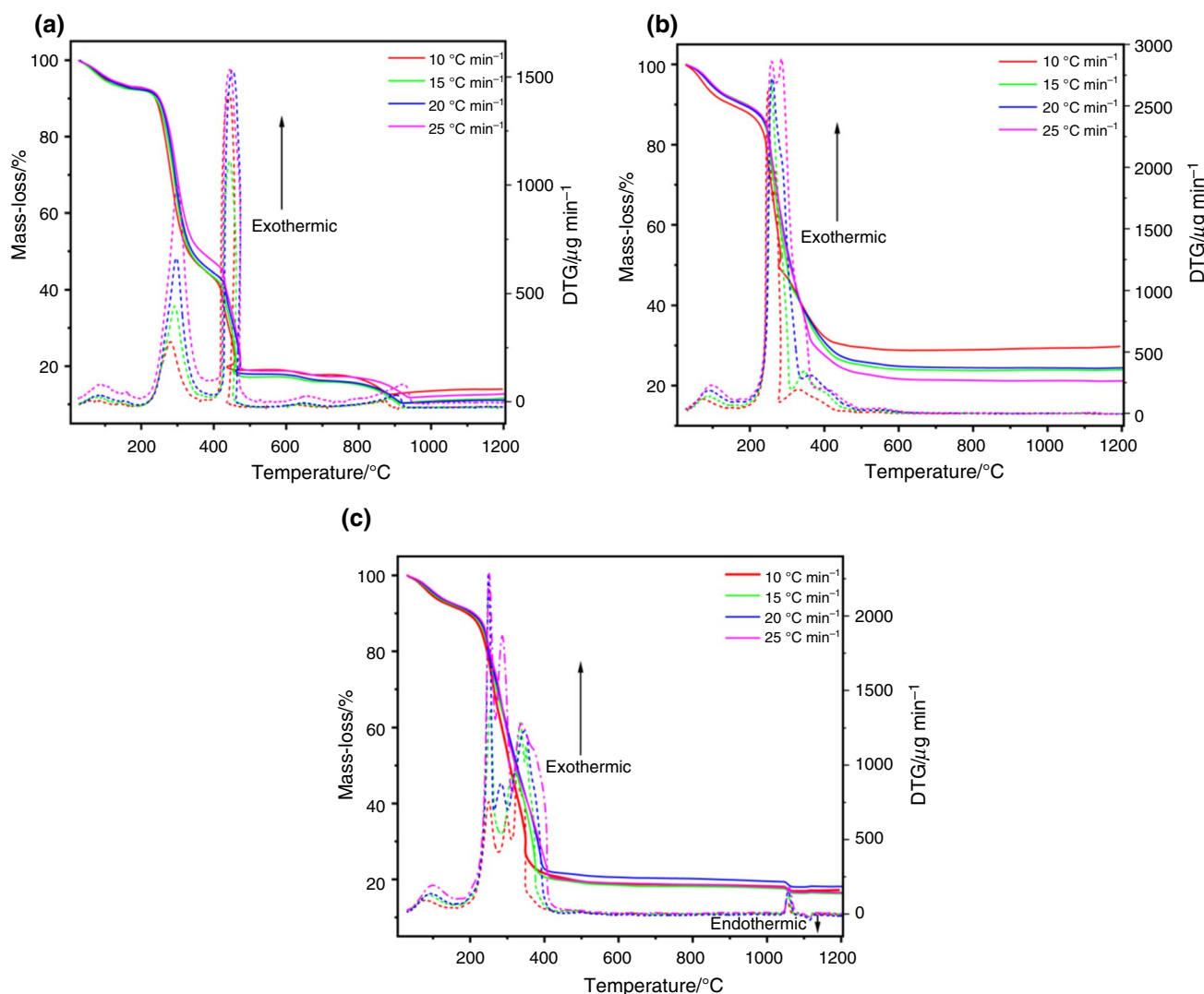


Fig. 4 TGA and DTG curves for **a** Raw water hyacinth, **b** Fe-impregnated water hyacinth, and **c** Cu-impregnated water hyacinth

DTG analysis was performed to study the thermal degradation behavior of samples in an inert atmosphere. Figure 4 shows the DTG curves of raw water hyacinth, Fe-impregnated, and Cu-impregnated water hyacinth samples at the same heating rates. From the curve, it can be concluded that hemicellulose and cellulose start degrading with the second exothermic peak between 200–300 °C and 230–330 °C, respectively [43]. In Fig. 4a, the small peak between 200 and 400 °C is due to the degradation of hemicellulose and cellulose overlapping as water hyacinth has lower crystallinity [44]. The lignin starts degrading with the third exothermic peak between 200 and 500 °C. DTG curve of raw water hyacinth shows the peak temperature of 437 °C at 10 °C min⁻¹, and the peak temperature further increases for the respective higher heating rates. A similar trend was also evident for the Fe and Cu-impregnated water hyacinth samples, but the peak temperature shifts toward lower temperature as the

former one shows the peak temperature of 277 °C and the latter one shows the peak temperature at 350 °C. Similar to TGA curves, DTG curves also show the first exothermic peak from 30 to 150 °C indicating mass loss due to moisture content and lighter volatile components. The degradation of cellulose and hemicellulose content into amorphous carbon atoms in the second clear exothermic peak range results in the reduction in the M⁺ to metallic metal nanoparticles.

Kinetic analysis

Activation energy calculation

The activation energy was determined by employing both differential (Friedman method) as well as integral (FWO, KAS, and Starink) isoconversional models. Plots of isoconversional methods for activation energy calculation form

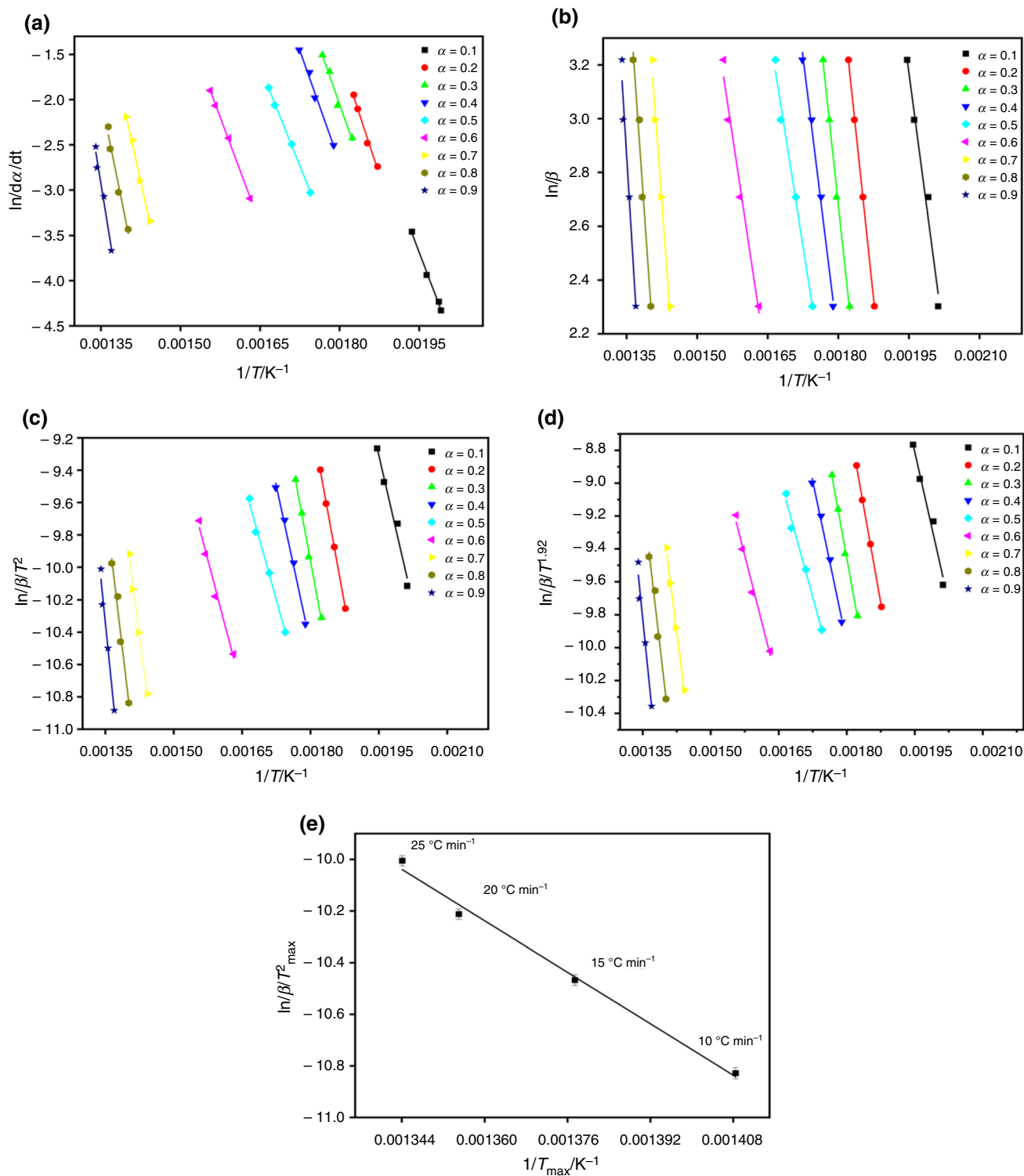


Fig. 5 Linear plots for calculation of Arrhenius parameter for Raw water hyacinth using **a** Friedman method, **b** FWO method, **c** KAS method, **d** Starink method, and **e** Kissinger method

the slope of equations in conversion varying in the range of 0.1–0.9 as represented in Figs. 5–7. Activation energies from distinct isoconversional methods for raw water

hyacinth, Fe–WH, and Cu–WH resulted in 138.0–173.9, 60.1–89.1, and 70.4–97.4 kJ mol⁻¹, respectively, as outlined in Tables 1–3. Huge variations in activation energy

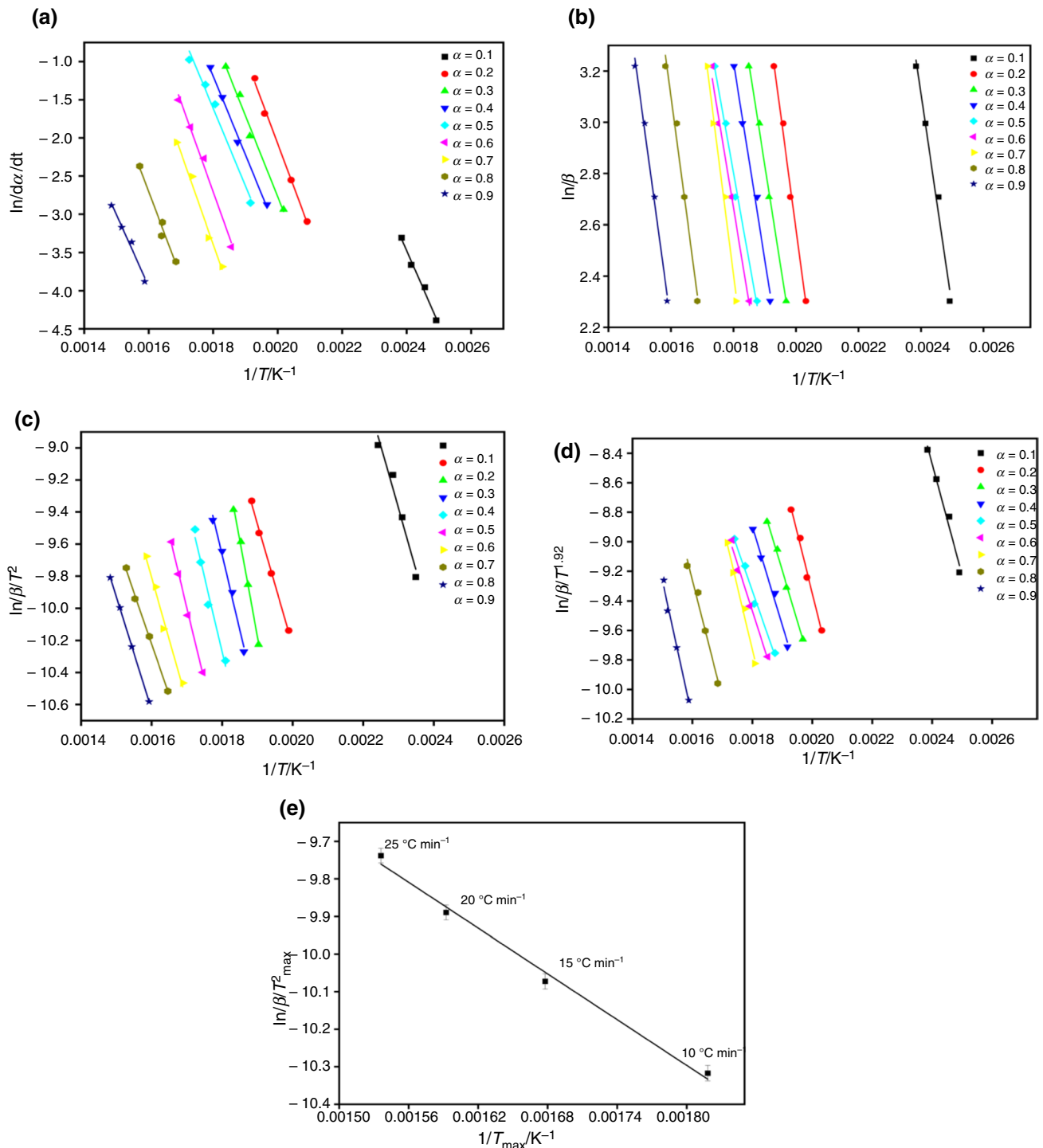


Fig. 6 Linear plots for calculation of Arrhenius parameter for Fe-impregnated water hyacinth using **a** Friedman method, **b** FWO method, **c** KAS method, **d** Starink method, and **e** Kissinger method

terms correspond to multiple complex reactions occurring during the thermal decomposition of the pyrolysis process [31]. The Friedman (differential) method resulted in higher activation energy than the integral methods of FWO, KAS, and Starink. The average activation energy for raw

water hyacinth was maximum with the Friedman method, followed by FWO, KAS, and Starink with 173.9, 141.0, 138.4, and 138.0 kJ mol⁻¹, respectively. In the case of Fe-impregnated water hyacinth, it followed the order of Friedman > FWO > Starink > KAS with the respective average

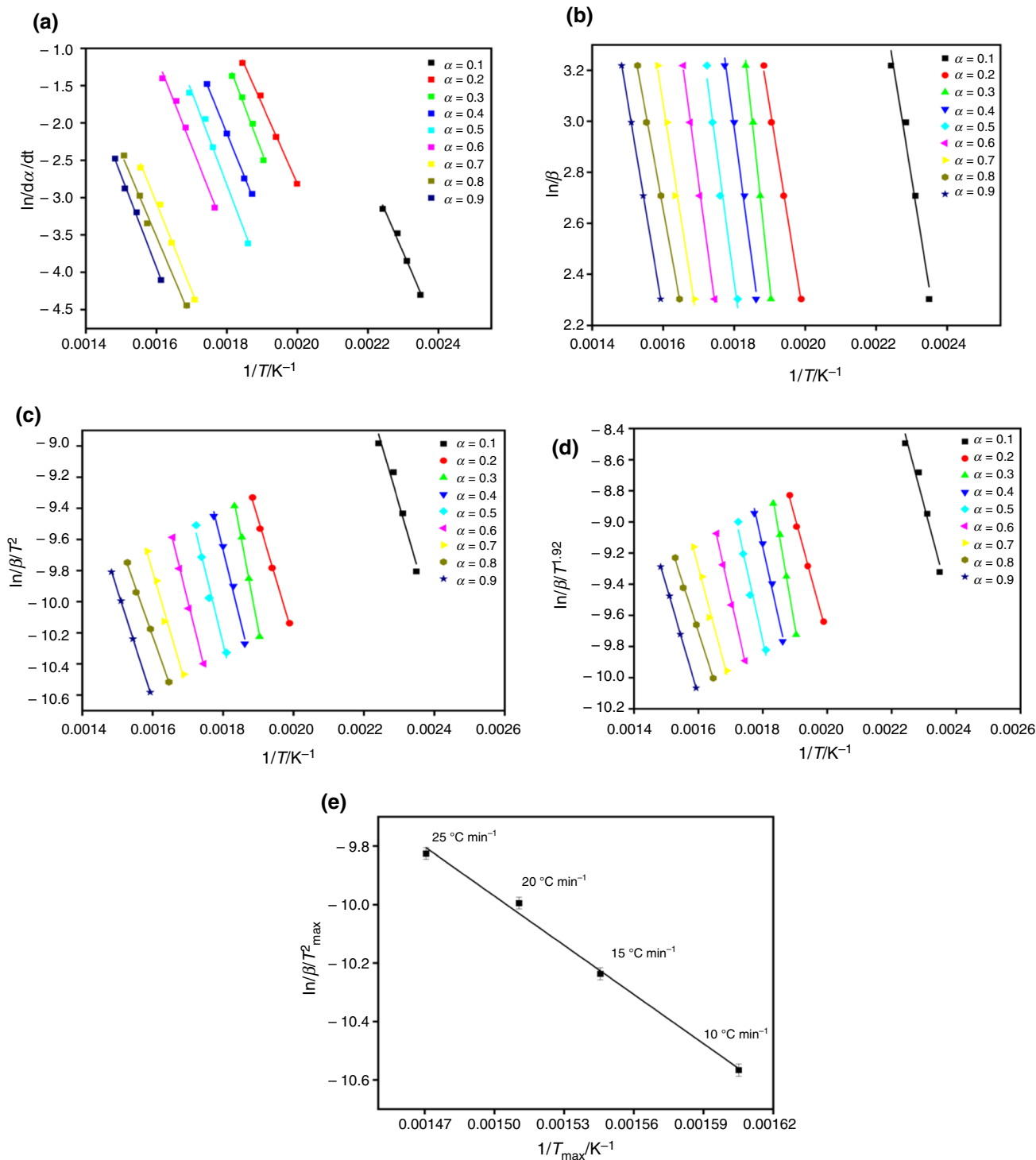


Fig. 7 Linear plots for calculation of Arrhenius parameter for Cu-impregnated water hyacinth using **a** Friedman method, **b** FWO method, **c** KAS method, **d** Starink method, and **e** Kissinger method

activation energy of 89.1, 65.8, 60.4, and 60.1 kJ mol⁻¹. The Cu-impregnated water hyacinth also followed a similar order with the average activation energy of 97.4 kJ mol⁻¹ (Friedman), 75.9 kJ mol⁻¹ (FWO), 70.7 kJ mol⁻¹ (Starink), and

70.4 kJ mol⁻¹ (KAS). The metal-impregnated water hyacinth resulted in lower activation energy for reaction in comparison with the raw water hyacinth.

Table 1 Activation energy, frequency factor, and thermodynamic parameters for Raw Water Hyacinth

Conversion (α)	Friedman method E_a /kJ mol ⁻¹	FWO method E_a /kJ mol ⁻¹	KAS method E_a /kJ mol ⁻¹	Starink method E_a /kJ mol ⁻¹	Frequency factor (A) /s ⁻¹	ΔH /kJ mol ⁻¹	ΔG /kJ mol ⁻¹	ΔS /kJ mol ⁻¹
0.1	128.4	104.4	101.5	101.7	2.4×10^{10}	124.3	166.5	-0.059
0.2	147.9	130.8	128.6	128.9	7.4×10^{11}	143.5	165.6	-0.031
0.3	138.8	128.8	126.2	126.6	1.5×10^{11}	134.3	166.0	-0.044
0.4	137.3	111.9	108.3	108.6	1.1×10^{11}	132.6	166.1	-0.047
0.5	121.1	87.9	84.1	83.1	6.5×10^9	116.4	166.8	-0.071
0.6	130.8	92.2	89.1	89.5	3.6×10^{10}	125.7	166.3	-0.057
0.7	219.5	187.4	179.5	179.9	2.0×10^{17}	213.8	163.3	0.071
0.8	240.9	198.3	196.6	197.0	8.4×10^{18}	235.0	162.7	0.101
0.9	300.2	226.9	231.8	226.8	2.4×10^{23}	294.1	161.4	0.186
Average	173.9	141.0	138.4	138.0	2.6×10^{22}	168.9	165.0	0.005

Table 2 Kinetics (activation energy and frequency factor) and thermodynamic parameters for Fe-impregnated Water Hyacinth

Conversion (α)	Friedman method E_a /kJ mol ⁻¹	FWO method E_a /kJ mol ⁻¹	KAS method E_a /kJ mol ⁻¹	Starink method E_a /kJ mol ⁻¹	Frequency factor (A) /s ⁻¹	ΔH /kJ mol ⁻¹	ΔG /kJ mol ⁻¹	ΔS /kJ mol ⁻¹
0.1	80.4	65.9	62.5	62.6	3.8×10^8	77.1	127.6	-0.091
0.2	94.2	72.2	67.5	67.9	9.0×10^9	90.2	126.9	-0.066
0.3	88.1	61.5	56.0	56.3	2.2×10^9	83.9	127.2	-0.078
0.4	85.6	60.9	55.1	55.4	1.3×10^9	81.4	127.3	-0.083
0.5	84.5	54.2	47.8	48.1	9.8×10^8	80.2	127.3	-0.085
0.6	98.1	58.7	52.5	52.8	2.2×10^{10}	93.8	126.8	-0.060
0.7	99.7	75.8	70.3	70.6	3.2×10^{10}	95.2	126.6	-0.057
0.8	93.0	72.3	65.9	66.3	7.0×10^9	88.1	126.9	-0.070
0.9	78.0	70.7	63.5	63.9	2.2×10^8	72.8	127.7	-0.099
Average	89.1	65.8	60.1	60.4	8.3×10^9	84.7	127.1	-0.076

Table 3 Estimation of parameters like activation energy, frequency factor, and thermodynamic parameters for Cu-impregnated Water Hyacinth

Conversion (α)	Friedman method E_a /kJ mol ⁻¹	FWO method E_a /kJ mol ⁻¹	KAS method E_a /kJ mol ⁻¹	Starink method E_a /kJ mol ⁻¹	Frequency factor (A) /s ⁻¹	ΔH /kJ mol ⁻¹	ΔG /kJ mol ⁻¹	ΔS /kJ mol ⁻¹
0.1	90.7	68.4	64.7	64.9	3.1×10^8	87.1	145.8	-0.094
0.2	88.3	68.1	63.1	63.4	1.9×10^8	84.1	145.9	-0.099
0.3	104.6	103.1	99.5	99.8	5.2×10^9	100.2	145.1	-0.072
0.4	96.8	82.2	77.3	77.6	1.1×10^9	92.4	145.5	-0.085
0.5	103.7	82.3	77.2	77.5	4.4×10^9	99.3	145.1	-0.073
0.6	99.5	81.6	76.1	76.4	1.9×10^9	94.8	145.3	-0.081
0.7	97.6	70.7	64.2	64.6	1.3×10^9	92.8	145.4	-0.084
0.8	92.8	60.5	53.2	53.6	4.8×10^8	87.89	145.7	-0.092
0.9	102.5	66.0	58.7	59.0	3.4×10^9	97.3	145.2	-0.076
Average	97.4	75.9	70.4	70.7	2.0×10^9	92.9	145.4	-0.084

The diversity of activation energy about conversion factor for samples by Friedman, FWO, KAS, and Starink models is

represented in Fig. 8. Activation energies by the Friedman model were employed in determining frequency factor (A)

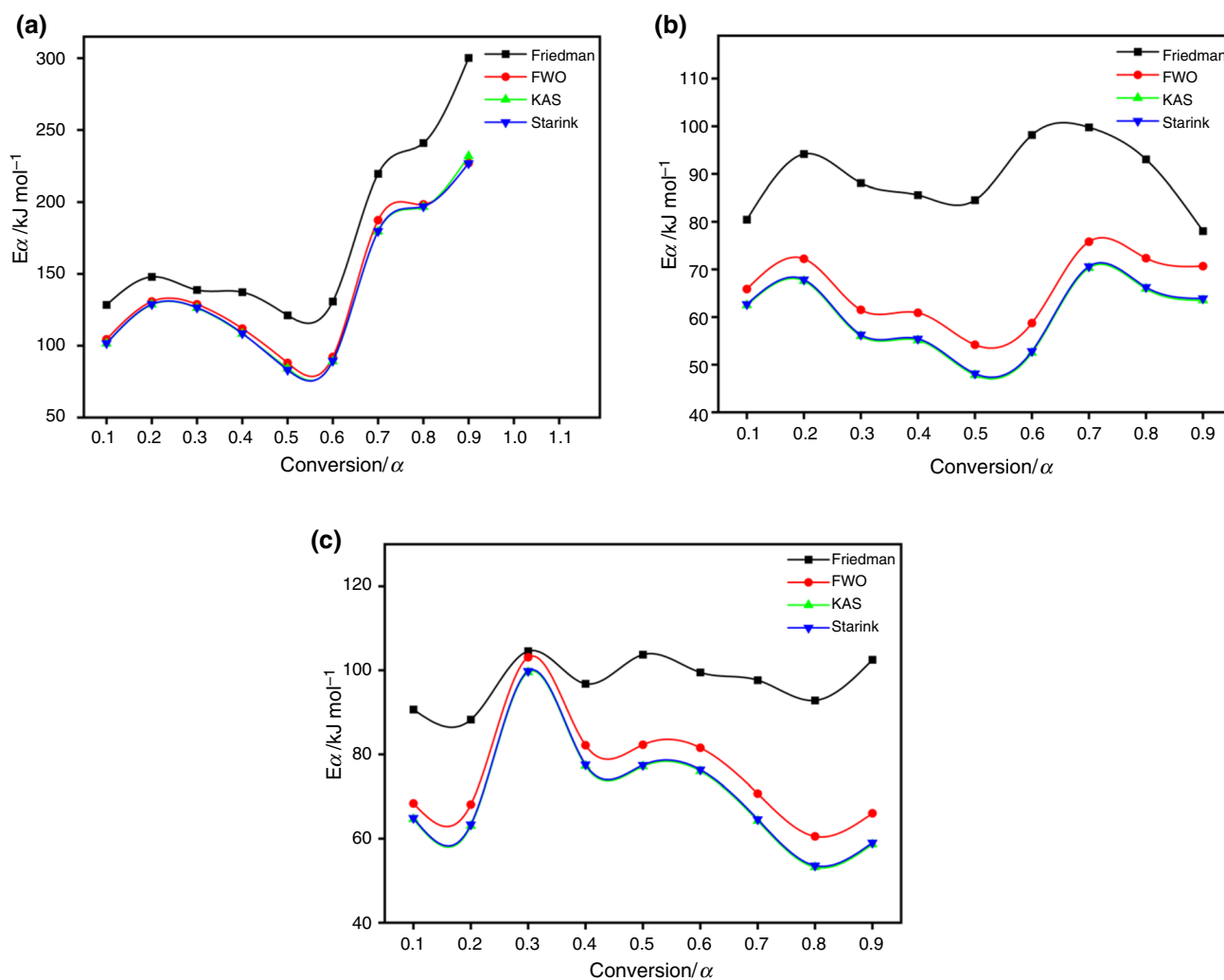


Fig. 8 Activation energy plots for **a** Raw water hyacinth, **b** Fe-impregnated water hyacinth, and **c** Cu-impregnated water hyacinth

and thermodynamic variables (ΔH_α , ΔG_α , and ΔS_α). It can be remarked that the activation energy vs. conversion plot is divided into three stages to conversion value, in the case of raw water hyacinth, (I) when $0.1 \leq \alpha \leq 0.2$, the activation energy value increases from 128.4 to 147.9 kJ mol⁻¹; (II) when $0.3 \leq \alpha \leq 0.6$, activation energy value remains constant within the range of 130.8–138.8 kJ mol⁻¹ and (III) when $\alpha \geq 0.7$, activation energy rapidly increases from 219.5 to 300.2 kJ mol⁻¹. Fe-WH sample shows the variation as, (I) when $0.1 \leq \alpha \leq 0.2$, activation energy value enhanced by 80.4–94.2 kJ mol⁻¹; (II) when $0.3 \leq \alpha \leq 0.6$, activation energy slightly varies within the range of 88.1 to 98.1 kJ mol⁻¹ and (III) when $\alpha \geq 0.7$, activation energy decreases from 99.7 to 78.0 kJ mol⁻¹. In case of Cu-WH samples shows a contradictory trend, (I) when $0.1 \leq \alpha \leq 0.2$, activation energy value decreases from 90.7 to 88.3 kJ mol⁻¹; (II) when $0.3 \leq \alpha \leq 0.6$, activation energy value remains almost constant within the range of 99.5–104.6 kJ mol⁻¹ and

(III) when $\alpha \geq 0.7$, activation energy increases from 97.6 to 102.5 kJ mol⁻¹. At higher values of degree of conversion, there might be the probability of secondary heterogeneous reactions taking place between gases and solid residue which further result in a rapid change in activation energy. The same trends were reported in the literature [31, 36]. Fe-impregnated and Cu-impregnated water hyacinth samples required lower activation energy as compared to raw water hyacinth as represented in Tables 1–3, signifying that raw water hyacinth required higher energy to break the chemical bonds of components, and hence, the reaction proceeds sluggishly.

Frequency factor calculation

The frequency factor (A) was examined by Kissinger's expression (Eq. 16) by utilizing activation energies calculated by Friedman, FWO, KAS, and Starink models.

Average frequency factor values for raw-WH, Fe-WH, and Cu-WH resulted in 2.6×10^{22} , 8.3×10^9 , and $2.0 \times 10^9 \text{ s}^{-1}$, respectively, as listed in Tables 1–3. A lower value of frequency factor ($A < 10^8 \text{ s}^{-1}$) indicates that the system is comparatively less reactive due to the high surface reactions, non-existence of an energy barrier, and complex transition state. The higher value of the frequency factor ($A \geq 10^8 \text{ s}^{-1}$) indicates a highly reactive system, the existence of an energy barrier, and the formation of a simple transition state. The frequency factor value within the range of 10^{10} – 10^{11} s^{-1} is mainly attributed to restriction in rotation [25, 31]. The wide variation in frequency factor value is a result of complex reactions taking place during the thermal degradation of biomass.

Thermodynamic parameters analysis

Thermodynamic variables, namely enthalpy change (ΔH_α), Gibbs-free energy change (ΔG_α), and entropy change (ΔS_α), were examined for corresponding activation energy and frequency factor as calculated by the Friedman method. Figure S1 (Supplementary File) presented the Change in enthalpy vs. Conversion plots, which shows the insignificant effect of heating rates as curves overlapped with each other. The plots of change in Gibbs free energy and entropy vs. conversion significantly vary with heating rates, as ΔG_α (Eq. 18) and ΔS_α (Eq. 19) depend upon the DTG curve's peak temperature, as shown in Fig. S2 and Fig. S3 (Supplementary File), respectively. The average value of ΔH_α in the thermal degradation process for raw water hyacinth, Fe-impregnated, and Cu-impregnated water hyacinth is 168.9, 84.7, and 92.9 kJ mol^{-1} , respectively, indicating the amount of energy consumed in the thermal decomposition of biomass to bio-oil, gas, and carbon material products. Less energy difference between ΔH_α and E_α ($\approx 5 \text{ kJ mol}^{-1}$) is reported further concluding favorable conditions for the formation of products due to the low energy barrier [45]. Change in enthalpy value is highest for raw water hyacinth, signifying the higher energy requirement for breaking reactants bonds, followed by Cu-impregnated water hyacinth and Fe-impregnated water hyacinth.

The average value of ΔG_α for the thermal degradation process for raw water hyacinth, Fe-impregnated, and Cu-impregnated water hyacinth is 165.0, 127.1, and 145.4 kJ mol^{-1} , respectively. A higher value of ΔG_α of raw water hyacinth represents unfavorable reactions demanding higher energy. On the other hand, the average value of change in entropy (ΔS_α) for the thermal degradation process for raw water hyacinth, Fe-impregnated, and Cu-impregnated water hyacinth is 0.005, -0.076 , and $-0.084 \text{ kJ mol}^{-1}$, respectively, with the negative values representing attainment of thermal equilibrium. The average positive value of ΔS_α for raw water hyacinth, as compared to the remaining two samples concluding

the system for the raw water hyacinth sample, is far from thermodynamic equilibrium. In the plot of ΔS_α vs. conversion of raw water hyacinth, as the conversion increases in the range of $0.1 \leq \alpha \leq 0.6$, the entropy change curve declines, representing the gradual decrease in reactivity with the rise in residence time to form activated intermediates. When $\alpha \geq 0.7$ again, the reactivity of the system increases. In the case of Fe-WH, entropy change decreases within the range of $0.1 \leq \alpha \leq 0.5$ conversion, increases from $0.5 \leq \alpha \leq 0.6$, and then, further decreases from $0.7 \leq \alpha \leq 0.9$. On the other hand, Cu-impregnated water hyacinth shows a continuous variation in entropy trend within the entire range of conversion of $0.1 \leq \alpha \leq 0.9$. Combining the thermodynamic parameters results, it is concluded that, in the initial stage of thermal decomposition, the system is most reactive with endothermic. As the degradation continues, the system becomes less reactive but due to the continuous supply of energy the free energy of the system increases.

Reaction mechanism by Z-Master plot

Reaction kinetics for the thermal degradation of raw and metal-impregnated water hyacinth with the varying conversion from 0.1 to 0.9 at a heating rate of $10 \text{ }^\circ\text{C min}^{-1}$ was predicted by the Z-Master plot approach. It compared the experimental data with the various theoretical reaction kinetic models as outlined in Table S1 (Supplementary File) is presented in Fig. 9 to describe the most predictable kinetic model. The Z-Master plots of raw water hyacinth follow the reaction order kinetic model, as the experimental curve overlaps the second- and third-order reaction model in conversion range of $\alpha \leq 0.5$ whereas, first-order reaction model for $\alpha > 0.5$ as shown in Fig. 9a. However, in the case of Fe-impregnated water hyacinth overlaps first- and second-order reaction model within the conversion range of $\alpha \leq 0.5$ followed by third-order reaction kinetic model for $\alpha > 0.5$ as best fitted by the kinetic model as represented in Fig. 9b. On the other hand, in Cu-impregnated water hyacinth, the experimental curve was close to the third-order reaction model indicating reaction kinetics within the conversion range of $\alpha \leq 0.5$, followed up by second- and third-order kinetics reaction model for $\alpha > 0.5$ as shown in Fig. 9c. The overall results conclude that as the conversion value increases from 0.1 to 0.5, the thermal degradation follows the second- and third-order reaction mechanism, and a further increase in conversion value from 0.7 up to 0.9 it follows the first-order reaction mechanism.

Experimental analysis

A pyrolysis experiment of metal-impregnated water hyacinth was conducted at $280 \text{ }^\circ\text{C}$ temperature for a reaction time of 15 min in a Parr reactor. The metal ions impregnated onto the

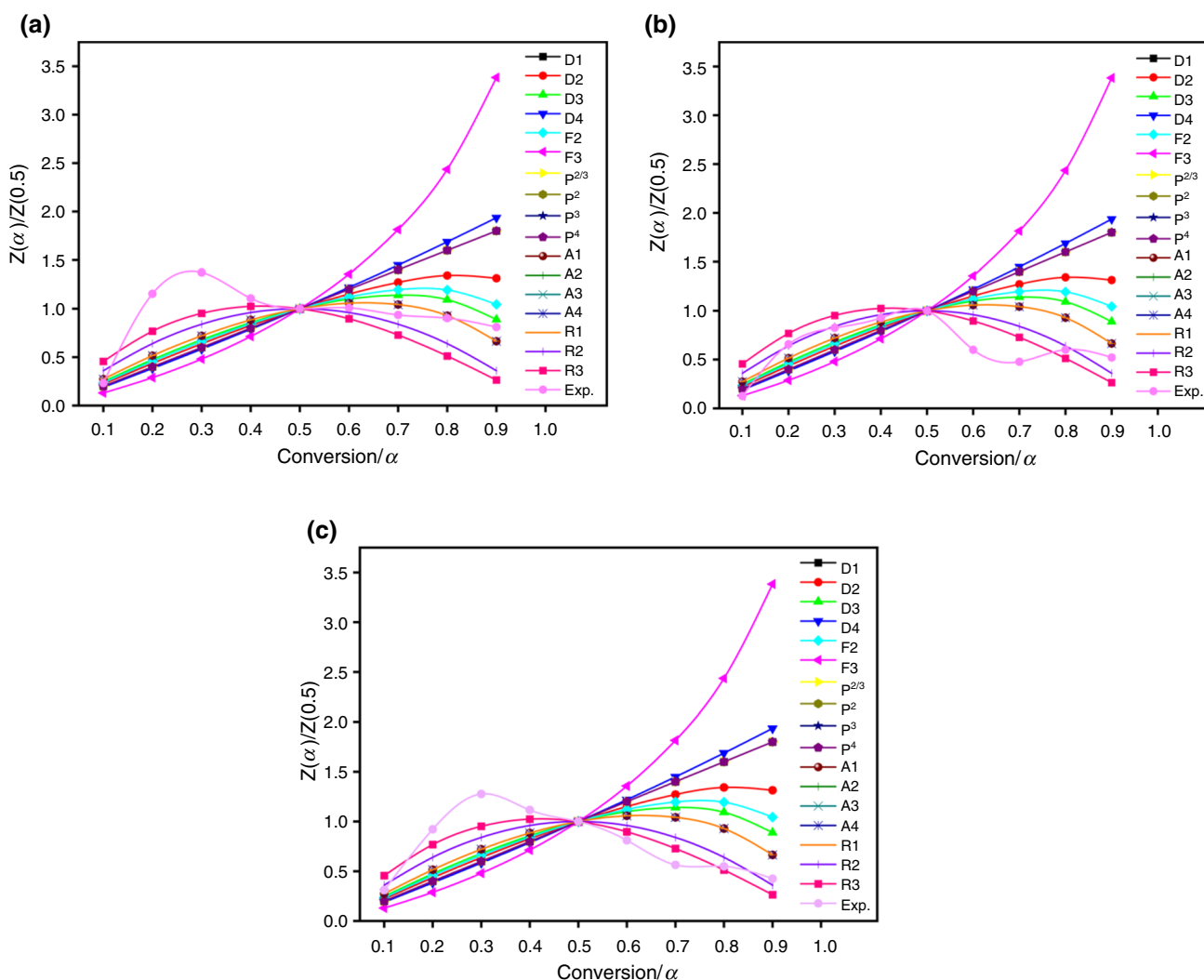


Fig. 9 Theoretical and experimental plots for determination of the physical mechanism of thermal degradation of water hyacinth using Z-Master plot **a** Raw water hyacinth, **b** Fe-impregnated water hyacinth, and **c** Cu-impregnated water hyacinth

biomass sample act as a catalyst during pyrolysis treatment to optimize the bio-oil yield. During pyrolysis, initially, dehydration and depolymerization reactions are the dominating reactions to convert the biomass monomers into intermediates. Pyrolysis of cellulose results in the cleavage of β-1,4-glycosidic bonds by dehydration reaction at high temperatures resulting in the formation of acids and alcohols. Hemicellulose is disrupted thermally at a lower temperature as compared to cellulose due to the amorphous nature of hemicellulose chains resulting in the formation of aldehyde, furans, and ketone by dehydration and isomerization reactions. The lignin is first depolymerized to its monomers as *p*-hydroxyphenyl propane, guaiacyl, and syringyl, and then, undergoes catalytic deoxygenation, dehydration, decarboxylation, and oligomerization reaction to form aromatics by cleavage of β-O-4, α-O-4 linkage and C–C and C–O bonds and then, repolymerization reaction to form carbon hybrid [46]. The pyrolysis of the

Fe-impregnated sample resulted in 23.4% of the total bio-oil yield comprising 17.7% as heavy oil and 5.7% as light oil, whereas Cu-impregnated water hyacinth resulted in a comparatively lower total bio-oil yield of 11.5% consisting of heavy oil as 7.7% and light oil as 3.8% as shown in Table S3 (Supplementary File). The Fe catalyst slightly enhances the conversion of hemicellulose at a lower temperature in comparison with the Cu catalyst resulting in higher bio-oil yield, whereas Cu catalyzes the reaction between lignin and active hydrogen to form phenolic compounds [47]. The metal–carbon hybrid of 32.1 and 52.2% for Fe-impregnated and Cu-impregnated samples, respectively, was observed by pyrolysis as repolymerization and recondensation reactions are more dominating in Cu-catalyzed samples resulting in higher metal–carbon yield as compared to Fe catalyzed sample. The Fe-impregnated sample resulted in a higher gaseous yield of 44.5% in comparison with the Cu-impregnated sample with a gas yield of 36.4% as

Fe promotes the pyrolysis efficiency and limits the formation of hydrocarbon as a result of polymerization, thus increasing the gaseous components to 44.5% by dehydrogenation of tar to form hydrogen and promoted both the water gas shift and Boudouard reactions [48]. The catalytic effect of Cu resulted in the decline in gaseous yield to 36.4% as Cu promoted the aromatization of C_xH_y of gas phase reaction to form aromatic compounds and hence, increased bio-oil yield at the expense of gas yield [17]. The literature reported the effect of various heterogeneous and homogeneous catalysts on bio-oil yield by thermal degradation. Pyrolysis of Fe-dispersed water hyacinth at 540 °C and 60 min reaction time resulted in the generation of synthesis gas and hydrogen production. They concluded that Fe plays a significant role in enhancing the gas yield with H₂-42%, CO₂-23%, CO-22%, and CH₄-7% [49]. Pyrolysis of Cu-polluted fir sawdust biomass resulted in enhanced bio-oil yield and high heating value of 54.3% and 14.79 MJ kg⁻¹, respectively, as compared to raw fir sawdust biomass. Pyrolysis of water hyacinth in the presence of Cu catalyst at 450 °C, the residence time of 60 min, and a heating rate of 1 °C s⁻¹ resulted in a bio-oil yield of 31.6% and conversion of 51.9% with the formation of aliphatic hydrocarbon in the range of C₇-C₂₀ [50]. Slow pyrolysis of Fe and Cu-contaminated *Avicennia marina* biomass was conducted to study the effect of temperature and deportment of heavy metals in pyrolysis products by varying the temperature from 300 to 800 °C. It was observed that more than 90% of Fe and Cu was retained in solid residue, concluding the non-volatile nature of Fe and Cu. Results showed a bio-oil yield of 0.5 and 0.3% with a gas yield of 94.4 and 93.3% at 800 °C for Fe and Cu contaminated biomass, respectively [51].

Kinetic parameters by TGA analysis were validated by pyrolysis experiments of Fe-WH, and Cu-WH samples at 280 °C and graphs were plotted. Each experimental run was performed thrice, and the average yield conversion was compared with the repeated kinetic simulation with error bars of standard deviation as shown in Fig. S4 (Supplementary File). It can be concluded from the plot that the model predicted by kinetic parameters and experimental data is in good agreement as the Fe-impregnated water hyacinth shows the conversion of 0.68 by pyrolysis experiment at 280 °C, whereas TGA analysis the conversion of 0.7 at the same temperature. In the case of Cu-impregnated water hyacinth, the pyrolysis experiment shows a conversion of 0.48 at 280 °C, and TGA analysis shows a conversion of 0.45 at the same temperature.

Conclusions

Pyrolytic experiments of Fe/Cu-loaded water hyacinth were conducted for the effect of the metals on the quantification of bio-oil yields. Fe (23.4%) has promoted the deoxygenation,

dehydration, decarboxylation, and isomerization reactions to a greater extent than Cu (11.5%) yielding higher bio-oil yields. The kinetic analysis and thermodynamic variables of raw and metal (Cu/Fe) impregnated water hyacinth were studied by comparing thermogravimetry data and various isoconversional models. Average activation energy as attained by the Friedman method for raw water hyacinth, Fe-WH, and Cu-WH resulted in 173.9, 89.1, and 97.4 kJ mol⁻¹, respectively. The average value of the frequency factor for raw water hyacinth, Fe-WH, and Cu-WH is noted as 2.6×10^{22} , 8.3×10^9 , and 2.0×10^9 s⁻¹, respectively. The most probable models for raw, Cu-WH, and Fe-WH were reaction-order models following the first-, second-, and third-order reaction kinetics varying with conversion. The values for ΔH_a and ΔG_a remain positive throughout the process concluding the endothermic nature with the high free energy of the system, whereas the ΔS_a value shows variation with conversion, negative from $0.1 \leq \alpha \leq 0.6$ and positive form $\alpha \geq 0.7$ with correspondingly varying the reactivity. Overall results of kinetics and thermodynamic parameters concluded that Fe and Cu-loaded water hyacinth required lower activation energy and Gibbs energy and have a high potential to be used as a feed raw material for bio-energy generation.

Supplementary Information The online version contains supplementary material available at <https://doi.org/10.1007/s10973-023-12573-8>.

Author's Contribution PY: She is a Ph.D. Student who have conducted experiments, kinetics and thermogravimetric study, analysis of the obtained data, preparation of figures and tables along with the manuscript. SNR: Development of concept, pyrolysis, Analysis of the generated data, and manuscript editing.

Funding The researchers are thankful to Science and Engineering Research Board, Government of India (Grant Number: CRG/2020/000360) for the financial support to perform the experiments under Core Research Grant.

Availability of data and materials The data and materials can be made available on request.

Declarations

Conflict of interest The authors declare that they have no known competing financial interests or personal relationships that could have appeared to influence the work reported in this paper.

Ethical Approval Not applicable.

References

1. de Caprariis B, Scarsella M, Bavasso I, Bracciale MP, Tai L, De Filippis P. Effect of Ni, Zn and Fe on hydrothermal liquefaction of cellulose: Impact on bio-crude yield and composition. *J Anal*

- Appl Pyrolysis. 2021;157: 105225. <https://doi.org/10.1016/j.jaap.2021.105225>.
2. Ibrahim M, Osman O, Mahmoud AA, Elhaes H. Spectroscopic analyses of water hyacinth: FTIR and modeling approaches. *Der Pharma Chem.* 2015;7:182–8.
 3. Tajvidi K, Pupovac K, Kükrek M, Palkovits R. Copper-based catalysts for efficient valorization of cellulose. *Chemsuschem.* 2012;5:2139–42. <https://doi.org/10.1002/cssc.201200482>.
 4. Yang J, (Sophia) He Q, Yang L. A review on hydrothermal co-liquefaction of biomass. *Appl Energy.* 2019;81:926–45. <https://doi.org/10.1016/j.rser.2017.05.178>.
 5. Okolie JA, Nanda S, Dalai AK, Kozinski JA. Chemistry and specialty industrial applications of lignocellulosic biomass. *Waste Biomass Valorization.* 2021;12:2145–69. <https://doi.org/10.1007/s12649-020-01123-0>.
 6. Mohan D, Pittman CU, Steele PH. Pyrolysis of wood/biomass for bio-oil: a critical review. *Energy Fuels.* 2006;20:848–89. <https://doi.org/10.1021/ef0502397>.
 7. Özsin G, Pütün AE. Insights into pyrolysis and co-pyrolysis of biomass and polystyrene: thermochemical behaviors, kinetics and evolved gas analysis. *Energy Convers Manag.* 2017;149:675–85. <https://doi.org/10.1016/j.enconman.2017.07.059>.
 8. Duan P, Xu Y, Wang F, Wang B, Yan W. Catalytic upgrading of pretreated algal bio-oil over zeolite catalysts in supercritical water. *Biochem Eng J.* 2016;116:105–12. <https://doi.org/10.1016/j.bej.2015.12.006>.
 9. Grilic M, Veryasov G, Likozar B, Jesih A, Levec J. Hydrodeoxygenation of solvolysed lignocellulosic biomass by unsupported MoS₂, MoO₃, Mo₂C and WS₂ catalysts. *Appl Catal B Environ.* 2015;163:467–77. <https://doi.org/10.1016/j.apcatb.2014.08.032>.
 10. Milina M, Mitchell S, Pérez-Ramírez J. Prospectives for bio-oil upgrading via esterification over zeolite catalysts. *Catal Today.* 2014;235:176–83. <https://doi.org/10.1016/j.cattod.2014.02.047>.
 11. Wang S, Cai Q, Zhang F, Li X, Zhang L, Luo Z. Hydrogen production via catalytic reforming of the bio-oil model compounds: acetic acid, phenol and hydroxyacetone. *Int J Hydrogen Energy.* 2014;39:18675–87. <https://doi.org/10.1016/j.ijhydene.2014.01.142>.
 12. Guna V, Ilangovan M, Anantha Prasad MG, Reddy N. Water hyacinth: a unique source for sustainable materials and products. *ACS Sustain Chem Eng.* 2017;5:4478–90. <https://doi.org/10.1021/acssuschemeng.7b00051>.
 13. Sindhu R, Binod P, Pandey A, Madhavan A, Alphonsa JA, Vivek N. Water hyacinth a potential source for value addition: an overview. *Bioresour Technol.* 2017;230:152–62. <https://doi.org/10.1016/j.biortech.2017.01.035>.
 14. Li F, He X, Srishti A, Song S, Tiang Wah Tan H, Sweeney DJ. Water hyacinth for energy and environmental applications: a review. *Bioresour Technol.* 2021;327:124809. <https://doi.org/10.1016/j.biortech.2021.124809>.
 15. Tavasoli A, Barati M, Karimi A. Conversion of sugarcane bagasse to gaseous and liquid fuels in near-critical water media using K₂O promoted Cu/γ-Al₂O₃-MgO nanocatalysts. *Biomass Bioenergy.* 2015;80:63–72. <https://doi.org/10.1016/j.biombioe.2015.04.031>.
 16. Kinata SE, Loubar K, Paraschiv M, Tazerout M, Belloncle C. Catalytic hydroliquefaction of charcoal CCB (copper, chromium and boron)-treated wood for bio-oil production: Influence of CCB salts, residence time and catalysts. *Appl Energy.* 2014;115:57–64. <https://doi.org/10.1016/j.apenergy.2013.10.057>.
 17. Liu WJ, Tian K, Jiang H, Zhang XS, Ding HS, Yu HQ. Selectively improving the bio-oil quality by catalytic fast pyrolysis of heavy-metal-polluted biomass: take copper (Cu) as an example. *Environ Sci Technol.* 2012;46:7849–56. <https://doi.org/10.1021/es204681y>.
 18. Singh R, Balagurumurthy B, Prakash A, Bhaskar T. Catalytic hydrothermal liquefaction of water hyacinth. *Bioresour Technol.* 2015;178:157–65. <https://doi.org/10.1016/j.biortech.2014.08.119>.
 19. Zhou C, Zhu X, Qian F, Shen W, Xu H, Zhang S. Catalytic hydrothermal liquefaction of rice straw in water/ethanol mixtures for high yields of monomeric phenols using reductive CuZnAl catalyst. *Fuel Process Technol.* 2016;154:1–6. <https://doi.org/10.1016/j.fuproc.2016.08.010>.
 20. Wang W, Yu Q, Meng H, Han W, Li J, Zhang J. Catalytic liquefaction of municipal sewage sludge over transition metal catalysts in ethanol-water co-solvent. *Bioresour Technol.* 2018;249:361–7. <https://doi.org/10.1016/j.biortech.2017.09.205>.
 21. Lee JH, Hwang H, Moon J, Choi JW. Characterization of hydrothermal liquefaction products from coconut shell in the presence of selected transition metal chlorides. *J Anal Appl Pyrolysis.* 2016;122:415–21. <https://doi.org/10.1016/j.jaap.2016.11.005>.
 22. Lee JH, Hwang H, Choi JW. Effects of transition metals on hydrothermal liquefaction of empty fruit bunches (EFB) for conversion to biofuel and valuable chemicals. *Energy.* 2018;162:1–9. <https://doi.org/10.1016/j.energy.2018.07.197>.
 23. Sarkar M, Rahman AKML, Bhoumik NC. Remediation of chromium and copper on water hyacinth (*E. crassipes*) shoot powder. *Water Resour Ind.* 2017;17:1–6. <https://doi.org/10.1016/j.wri.2016.12.003>.
 24. Yang S, Zhang X, Chen L, Sun L, Xie X, Zhao B. Production of syngas from pyrolysis of biomass using Fe/CaO catalysts: effect of operating conditions on the process. *J Anal Appl Pyrolysis.* 2017;125:1–8. <https://doi.org/10.1016/j.jaap.2017.05.007>.
 25. Dhyani V, Kumar J, Bhaskar T. Thermal decomposition kinetics of sorghum straw via thermogravimetric analysis. *Bioresour Technol.* 2017;245:1122–9. <https://doi.org/10.1016/j.biortech.2017.08.189>.
 26. Zhu H, Liu N. Kinetic analysis based on the kinetic compensation effect and optimization calculation. *Thermochim Acta.* 2020;690:178686. <https://doi.org/10.1016/j.tca.2020.178686>.
 27. Cai J, Xu D, Dong Z, Yu X, Yang Y, Banks SW. Processing thermogravimetric analysis data for isoconversional kinetic analysis of lignocellulosic biomass pyrolysis: case study of corn stalk. *Renew Sust Energy Rev.* 2018;82:2705–15. <https://doi.org/10.1016/j.rser.2017.09.113>.
 28. Martín-lara MÁ, Iáñez-rodríguez I, Blázquez G, Quesada L, Pérez A. Kinetics of thermal decomposition of some biomasses in an inert environment. An investigation of the effect of lead loaded by biosorption. *Waste Manage.* 2017;70:101–13. <https://doi.org/10.1016/j.wasman.2017.09.021>.
 29. Soria-verdugo A, Goos E, García-hernando N, Riedel U. Analyzing the pyrolysis kinetics of several microalgae species by various differential and integral isoconversional kinetic methods and the distributed activation energy model. *Algal Res.* 2018;32:11–29. <https://doi.org/10.1016/j.algal.2018.03.005>.
 30. Tabal A, Barakat A, Aboulkas A, El K. Pyrolysis of ficus nitida wood: determination of kinetic and thermodynamic parameters. *Fuel.* 2021;283: 119253. <https://doi.org/10.1016/j.fuel.2020.119253>.
 31. Hihu Muigai H, Choudhury BJ, Kalita P, Moholkar VS. Physico-chemical characterization and pyrolysis kinetics of Eichhornia Crassipes, Vetetia Peruviana, and Saccharum Officinarum. *Fuel.* 2021;289: 119949. <https://doi.org/10.1016/j.fuel.2020.119949>.
 32. Cortés AM, Bridgwater AV. Kinetic study of the pyrolysis of miscanthus and its acid hydrolysis residue by thermogravimetric analysis. *Fuel Process Technol.* 2015;138:184–93. <https://doi.org/10.1016/j.fuproc.2015.05.013>.
 33. Ma P, Yang J, Xing X, Wehrich S, Fan F, Zhang X. Isoconversional kinetics and characteristics of combustion on hydrothermally treated biomass. *Renew Energy.* 2017;114:1069–76. <https://doi.org/10.1016/j.renene.2017.07.115>.

34. Huang L, Liu J, He Y, Sun S, Chen J, Sun J. Thermodynamics and kinetics parameters of co-combustion between sewage sludge and water hyacinth in CO₂/O₂ atmosphere as biomass to solid biofuel. *Bioresour Technol.* 2016;218:631–42. <https://doi.org/10.1016/j.biortech.2016.06.133>.
35. Chandrasekaran A, Ramachandran S, Subbiah S. Determination of kinetic parameters in the pyrolysis operation and thermal behavior of *Prosopis juliflora* using thermogravimetric analysis. *Bioresour Technol.* 2017;233:413–22. <https://doi.org/10.1016/j.biortech.2017.02.119>.
36. Mallick D, Bora BJ, Baruah D, Barbhuiya SA, Banik R, Garg J. Mechanistic investigation and thermal degradation of eichhornia crassipes using thermogravimetric analysis. *SSRN Electron J.* 2020. <https://doi.org/10.2139/ssrn.3668845>.
37. Kumar SAP, Nagarajan R, Prasad KM, Anand B. Thermogravimetric study and kinetics of banana peel pyrolysis : a comparison of 'model-free' methods. *Biofuels.* 2019;0:1–10. <https://doi.org/10.1080/17597269.2019.1647375>.
38. Yadav P, Reddy SN. Hydrothermal liquefaction of Fe-impregnated water hyacinth for generation of liquid bio-fuels and nano Fe carbon hybrids. *Bioresour Technol.* 2020;313: 123691. <https://doi.org/10.1016/j.biortech.2020.123691>.
39. Rotaru R, Savin M, Tudorachi N, Peptu C, Samoila P, Sacarescu L. Ferromagnetic iron oxide-cellulose nanocomposites prepared by ultrasonication. *Polym Chem Roy Soc Chem.* 2018;9:860–8. <https://doi.org/10.1039/C7PY01587A>.
40. Wauton I, Ogbeide SE. Determination of the activation energy of water hyacinth (*Eichornia crassipes*) pyrolysis. *Int J Green Energy.* 2019;16:1571–6. <https://doi.org/10.1080/15435075.2019.1677236>.
41. Zhang B, Lin Q, Zhang Q, Wu K, Pu W, Yang M. Catalytic hydrothermal liquefaction of *Euglena* sp. microalgae over zeolite catalysts for the production of bio-oil. *RSC Adv Roy Soc Chem.* 2017;7:8944–51. <https://doi.org/10.1039/C6RA28747F>.
42. Gollakota ARK, Kishore N, Gu S. A review on hydrothermal liquefaction of biomass. *Renew Sust Energ Rev.* 2018;81:1378–92. <https://doi.org/10.1016/j.rser.2017.05.178>.
43. Yang X, Zhao Y, Li R, Wu Y, Yang M. A modified kinetic analysis method of cellulose pyrolysis based on TG–FTIR technique. *Thermochim Acta.* 2018;665:20–7. <https://doi.org/10.1016/j.tca.2018.05.008>.
44. Zhong S, Zhang B, Liu C, Shujaa aldeen A. Mechanism of synergistic effects and kinetics analysis in catalytic co-pyrolysis of water hyacinth and HDPE. *Energy Convers Manag.* Elsevier Ltd. 2021;228:113717. <https://doi.org/10.1016/j.enconman.2020.113717>.
45. Vuppaladadiyam AK, Zhao M, Memon MZ, Soomro AF. Microalgae as a renewable fuel resource: A comparative study on the thermogravimetric and kinetic behavior of four microalgae. *Sustain Energy Fuels Royal Soc Chem.* 2019;3:1283–96. <https://doi.org/10.1039/C9SE00114J>.
46. Zadeh ZE, Abdulkhani A, Aboelazayem O, Saha B. Recent insights into lignocellulosic biomass pyrolysis: a critical review on pretreatment, characterization, and products upgrading. *Processes.* 2020;8:31. <https://doi.org/10.3390/pr8070799>.
47. Shao J, Yan R, Chen H, Yang H, Ho D. Catalytic effect of metal oxides on pyrolysis of sewage sludge. *Fuel Process Technol.* 2010;91:1113–8. <https://doi.org/10.1016/j.fuproc.2010.03.023>.
48. Liu Y, Guo F, Li X, Li T, Peng K, Guo C. Catalytic effect of iron and nickel on gas formation from fast biomass pyrolysis in a micro fluidized bed reactor: a kinetic study. *Energy Fuels.* 2017;12278–87. <https://doi.org/10.1021/acs.energyfuels.7b02214>.
49. Tran TK, Kim N, Leu HJ, Pham MP, Luong NA, Vo HK. The production of hydrogen gas from modified water hyacinth (*Eichornia Crassipes*) biomass through pyrolysis process. *Int J Hydrogen Energy.* 2021;46:13976–84. <https://doi.org/10.1016/j.ijhydene.2020.08.225>.
50. Gulab H, Hussain K, Malik S, Hussain M. Effect of process conditions on bio-oil composition and production from catalytic pyrolysis of water hyacinth biomass. *Waste Biomass Valorization.* 2019;10:2595–609. <https://doi.org/10.1007/s12649-018-0238-5>.
51. He J, Strezov V, Kan T, Weldekidan H, Asumadu-Sarkodie S, Kumar R. Effect of temperature on heavy metal(loid) deportment during pyrolysis of *Avicennia marina* biomass obtained from phytoremediation. *Bioresour Technol.* 2019;278:214–22. <https://doi.org/10.1016/j.biortech.2019.01.101>.

Publisher's Note Springer Nature remains neutral with regard to jurisdictional claims in published maps and institutional affiliations.

Springer Nature or its licensor (e.g. a society or other partner) holds exclusive rights to this article under a publishing agreement with the author(s) or other rightsholder(s); author self-archiving of the accepted manuscript version of this article is solely governed by the terms of such publishing agreement and applicable law.